ADVANCED ENERGY MATERIALS
www.advenergymat.de

Revolutionizing Oxygen Evolution Reaction Catalysts: Efficient and Ultrastable Interstitial W-Doped NiFe-LDHs/MOFs through Controlled Topological Conversion of Metal-Organic Frameworks

Yiwei Bao, Xiongyi Liang, Hao Zhang, Xiuming Bu, ZiYan Cai, Yikai Yang, Di Yin, Yuxuan Zhang, Lijie Chen, Cheng Yang, Xiulan Hu,* Xiao Cheng Zeng, Johnny C Ho,* and Xianying Wang**

Although metal-organic frameworks (MOFs) show promise as electrocatalysts due to their unique intrinsic features, their activity and stability often fall short. Herein, NiFe-MOFs is used as a model to introduce group VIB metalates (Na_2WO_4, Na_2CrO_4, and Na_2MoO_4) into the topological conversion process of layer double hydroxide (LDHs)/MOFs, creating a series of interstitial VIB element-doped LDHs/MOFs catalysts. The metalates engage in the alkaline hydrolysis process of MOF, generating LDHs on the MOF surface. Furthermore, altering the pH value in the reaction environment can modify the catalysts' morphology, dopant/LDHs content, and electronic structure. Consequently, the prepared interstitial W-doped NiFe-LDHs/MOFs catalyst displays superior catalytic performance, with overpotentials of only 250 mV at 500 mA cm^{-2}. Moreover, a homemade anion-exchange membrane water electrolysis (AEMWE) system featuring the fabricated electrocatalyst as the anode can operate stably for 500 hours at 1 A cm^{-2}. The exceptional catalytic activity and stability stem from optimized intermediate adsorption/desorption behavior and the unique LDHs/MOFs nanostructure. This work not only highlights the potential of the catalysts for practical applications but also offers a new design approach for modulating MOFs using an alkaline hydrolysis strategy.

1. Introduction

Anion-exchange membrane water electrolysis (AEMWE) is garnering significant attention as a potentially eco-friendly and cost-effective technology for hydrogen production.[1,2] However, the slow kinetics of the oxygen evolution reaction (OER) at the anode significantly increases the overpotential during AEMWE operation, leading to increased energy consumption.[3–5] Among various candidates, NiFe-based metal-organic framework materials (MOFs) have been extensively explored as efficient non-precious metal OER catalysts. They are seen as potential replacements for existing Ru- and Ir-based oxide catalysts, thanks to their accessible metal sites, tunable porosity, and well-defined periodic framework structures.[6–8]

Nevertheless, MOFs reported to date still suffer from intrinsically low activity. Specifically, the weak stability of

Y. Bao, H. Zhang, X. Hu
College of Materials Science and Engineering
Nanjing Tech University
Nanjing 211816, China
E-mail: whoxiulan@njtech.edu.cn

The ORCID identification number(s) for the author(s) of this article can be found under https://doi.org/10.1002/aenm.202401909

DOI: 10.1002/aenm.202401909

Y. Bao, H. Zhang, X. Bu, Z. Cai, Y. Yang, X. Wang
CAS Key Laboratory of Materials for Energy Conversion
Shanghai Institute of Ceramics
Chinese Academy of Sciences
Shanghai 200050, China
E-mail: buxiuming@mail.sic.ac.cn; wangxianying@mail.sic.ac.cn

X. Liang, D. Yin, Y. Zhang, X. C. Zeng, J. C Ho
Department of Materials Science & Engineering
City University of Hong Kong
Hong Kong SAR 999077, China
E-mail: johnnyho@cityu.edu.hk

X. Liang
Shenzhen Research Institute
City University of Hong Kong
Shenzhen 518057, China

organic ligands in the MOFs can cause severe structural collapse and reconstruction during the AEMWE working conditions.[9–11] The MOFs/layered double hydroxides (LDHs) heterostructure, which involves the in situ topological conversion of MOFs to LDHs on the MOFs surface, presents a promising strategy to address these issues. This process preserves the well-maintained porous channels and increases the accessibility of LDHs.[12] The topological conversion of MOFs to LDHs process consists of two main steps: first, the cations in the MOFs undergo a hydrolysis reaction, and then the organic ligands are substituted by hydroxide ions to form the LDHs. This is due to the difference in the solubility product constant between hydroxides and MOFs.[13,14] For example, Huo reported the construction of LDHs/MOFs hierarchical hybrids, and the characterization results proved that a high hydroxide ion concentration can induce the gradual conversion of MOFs to LDHs.[15] In any case, finely regulating the composition and morphology of LDHs/MOFs by relying solely on the ion exchange reactions between hydroxide ions and organic ligands is challenging. This is because the concentration of hydroxide ions in near-neutral bases remains relatively unchanged. Inspired by this, introducing an additional ion into the topological conversion process of MOFs to LDHs may be a feasible option to fine-tune the morphology and composition of LDHs/MOFs heterostructures.

In this work, using NiFe-MOFs as a template, we prove that the morphology and composition of NiFe-MOFs/LDHs can be fine-tuned by introducing group VIB metalates (MO_4^{2-}: CrO_4^{2-}, MoO_4^{2-}, and WO_4^{2-}) during the MOFs/LDHs topological conversion process. According to the XRD results and synchrotron radiation characterization, the topological conversion process is facilitated by the involvement of metalates, which results in the formation of interstitial VIB element-doped LDHs/MOFs catalysts. More importantly, the morphology, dopant/LDHs content, and electronic structure of the LDHs/MOFs heterojunction structure can be altered by the modulation of hydroxide ions. Ultimately, the optimized interstitial W-doped NiFe- LDHs/MOFs hybrids show exceptional and ultra-stable OER performance; only a small overpotential of 250 mV is required to achieve a current density of 500 mA cm^{-2} with a Tafel slope 60.6 mV dec^{-1} in 1 M KOH. It is worth mentioning that the optimized catalysts can operate stably for 500 hours at a current density of 1 A cm^{-2} in a homemade AEMWE system. Our findings not only offer an efficient and stable electrocatalyst but also provide valuable insights for further improving the MOF catalyst performance through alkaline hydrolysis.

2. Result and Discussion

The process for preparing NiFeM-BDC/NF is illustrated in **Figure 1a**, and the detailed preparation process is shown in Supporting Information. Using the hydrothermal method, the NiFe-BDC precursor is typically synthesized on nickel foam with Ni^{2+}, Fe^{2+}, and terephthalic acid (BDC). Subsequently, the NiFe-BDC/NF is immersed in a metalate solution (including Na_2WO_4, Na_2CrO_4, and Na_2MoO_4) to fabricate the final electrocatalyst. The morphologies of NiFe-BDC and corresponding NiFeM-BDC were initially characterized by scanning electron microscopy (SEM). The NiFe-BDC sample displays a stacking layered nanosheet structure (Figure 1b). Following the ion-exchange process with various metalates, all NiFeM-BDC samples exhibit the same stacking layered nanosheet structure as the original NiFe-BDC, which indicates that the ion-exchange process has an insignificant impact on the morphology, as shown in Figure 1c–e. Moreover, due to the limited detection depth (≈ 10 nm), the atomic ratio results from the X-ray photoelectron spectroscopy (XPS) can provide a more reliable result on the nickel foam.[16] Specifically, the atomic ratio of metallic elements in several materials within NiFeM-BDC is as follows: W (0.6%) < Mo (7.6%) < Cr (15.8%). The order of the atomic ratio of heteroatoms in NiFe-BDC is consistent with the order of the dissociation constant (pK_a) magnitude of the metalate: pK_a (Na_2WO_4) = 2.7×10^{-13} < pK_a (Na_2MoO_4) = 1×10^{-8} < pK_a (Na_2CrO_4) = 1.4×10^{-7}, proving that the doping ratio is mainly controlled by the magnitude of pK_a. Then, taking NiFeW-BDC as an example, atomic force microscopy (AFM) and transmission electron microscopy (TEM) were further employed to confirm that the synthesized NiFeW-BDC is composed of stacked nanosheets with a thickness of about 1.5 nm (Figure 1f,g). Additionally, the energy dispersive spectroscopy (EDS) element mapping of NiFeW-BDC demonstrates that the elements of Ni, Fe, W, and C are present and uniformly distributed in the sample, confirming the successful preparation of NiFeW-BDC (Figure 1h–m). Furthermore, as shown in the full XPS spectrum (Figure S1, Supporting Information), in addition to the sharp peaks of Ni 2p, Fe 2p, O 1s, and C1s, the peaks of W 4f (35.52 eV), Mo 3d (232.18 eV), and Cr 2p (588.08 eV) can also be observed, which fully indicates the successful synthesis of NiFeM-BDC.

At the same time, identifying the presence form in which the metalate (CrO_4^{2-}, MoO_4^{2-}, and WO_4^{2-}) exists in NiFeM-BDC is essential. First, X-ray diffraction (XRD) patterns demonstrate that NiFe-BDC/NF and NiFeM-BDC/NF have the same crystal structure as nickel-based MOFs (**Figure 2a**). Also, the enlarged image in Figure 2b indicates that all NiFeM-BDC samples exhibit no peak shift, suggesting that the metalate ions are not in the form of intercalation.[17,18] More importantly, no $NiMO_4$ or $FeMO_4$ characteristic peaks are observed in the XRD pattern because a trace

X. Liang
Chengdu Research Institute
City University of Hong Kong
Chengdu 610200, China
L. Chen
CIMC Offshore Co., Ltd.
Shenzhen 518000, China
C. Yang
Institute of Materials Research
Tsinghua Shenzhen International Graduate School
Shenzhen 518055, China
J. C Ho
State Key Laboratory of Terahertz and Millimeter Waves
City University of Hong Kong
Hong Kong SAR 999077, China
J. C Ho
Institute for Materials Chemistry and Engineering
Kyushu University
Fukuoka 816 8580, Japan

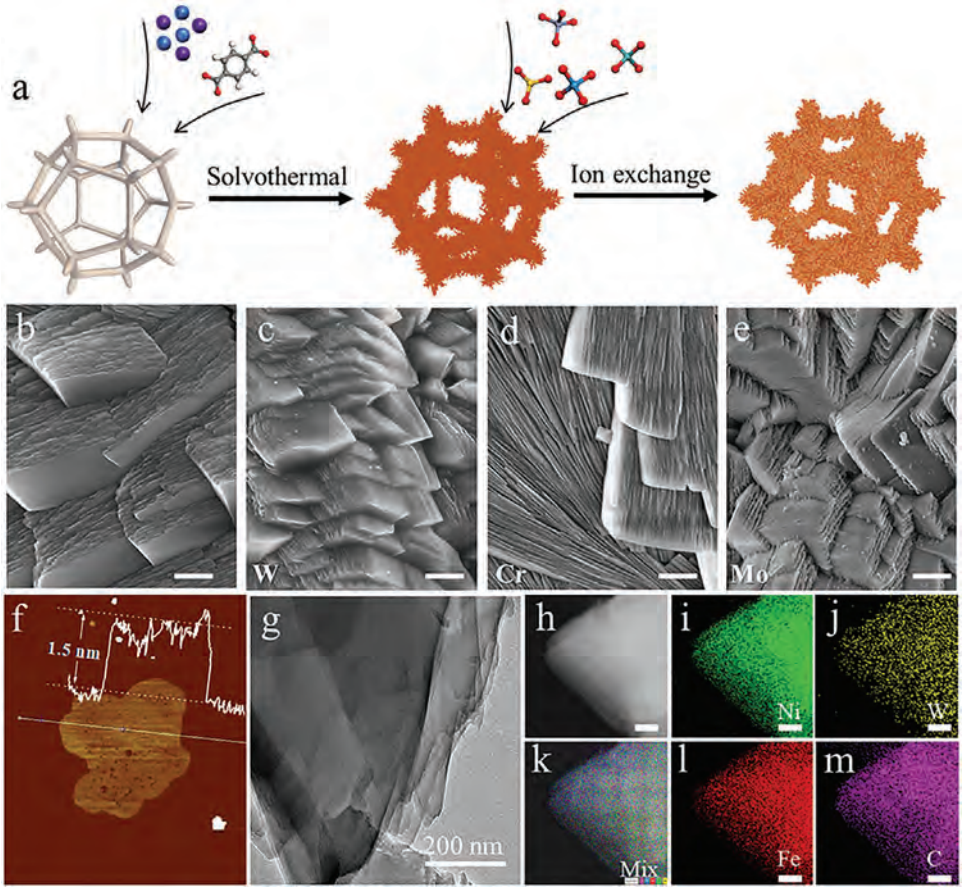

Figure 1. a) Schematic of the NiFeM-BDC preparation (M including W, Cr, Mo) on the nickel foam substrate. Blue represents Ni, purple represents Fe, red represents O, white represents H, gray represents C, dark blue represents W, light blue represents Cr, gray represents Mo; SEM images of b) NiFe-BDC, c) NiFeW-BDC, d) NiFeCr-BDC and e) NiFeMo-BDC; The scale bar in the (b–e) is 100 nm; f) AFM image of the NiFeW-BDC and the corresponding (g) TEM image; h–m) element mapping images, including Ni, W, Fe, C, and mix, respectively.

amount of metalate is added, suggesting the reaction between metalate and cations may not follow Equation 1.[19]

$$NiFe^{2+} + MO_4^{2-} \leftrightharpoons NiFe\left(MO_4\right) \quad (1)$$

Furthermore, in Figure 2c, the O 1s spectrum of the fabricated samples shows three typical characteristic peaks, including 532.78 eV (absorbed water), 531.08 eV (C-O) and 529.58 eV (metal-O), respectively.[10] Compared with NiFe-BDC, the significantly increased metal-O peak intensity indicates the formation of metal hydroxide. Because of the larger pK_a of Na_2CrO_4, the higher hydroxide concentration in the precursor solution during the preparation process increases the metal hydroxide product content on the MOF surface (Equations 2 and 3).

$$Na_2CrO_4 + 2H_2O \leftrightharpoons 2Na^+ + 2OH^- + H_2CrO_4 \quad (2)$$

$$NiFe^{2+}(BDC) + 2Na^+ + 2OH^- \leftrightharpoons NiFe(OH)_2 + Na_2BDC \quad (3)$$

To further confirm the present form of metalate, X-ray absorption fine structure analysis was employed to explore the local structure and chemical states. The X-ray absorption near edge structure (XANES) showed a slight attenuation of both Ni K-edge and Fe K-edge in NiFeW-BDC compared to the pristine NiFe-BDC samples, suggesting a lower valence state for both Ni and Fe states (Figure 2d,e). For the W L-edge spectra, the W atom in the NiFeW-BDC sample connects with oxygen atoms (Figure 2f). Then, the corresponding R-space extended X-ray absorption fine structure (EXAFS) spectra are explored. In the Ni K-edge EXAFS spectra, the prominent peaks at 1.5 Å for both NiFe-BDC and NiFeW-BDC are associated with Ni—O bonds (Figure 2g). The Fe K-edge EXAFS spectra of the NiFe-BDC and NiFeW-BDC samples revealed three significant peaks: Fe-O (1.97), Fe-Fe (2.68) and Fe-Fe1 (2.93) (Figure 2h). Further, based on the fitting results, the Ni active site's coordination number shows a minor change (from 6.3 ± 0.8 in NiFe-BDC to 6.4 ± 1.4 in NiFeW-BDC). In contrast, the coordination number of Fe significantly changed (Tables S1 and S2, Supporting Information). Specifically, the coordination numbers for Fe-O, Fe-Fe, and Fe-Fe1 changed from 4.4 ± 0.3 to 4.6 ± 0.3, 3.0 ± 1.1 to 3.2 ± 1.1, and 7.0 ± 1.1 to 6.3 ± 0.9, respectively. Only the W—O bond located at 1.3 Å is detected in the W L-edge EXAFS spectra, with no observable W—W bond peak in NiFeW-BDC, and the coordination number is 2.7 ± 0.6 (Figure 2i, Table S3, Supporting Information). The coordination number of the W (2.7 ± 0.6) is totally different from the Ni (6.4 ± 1.4) and Fe (4.6 ± 0.3). As we know, there are two types of heteroatom

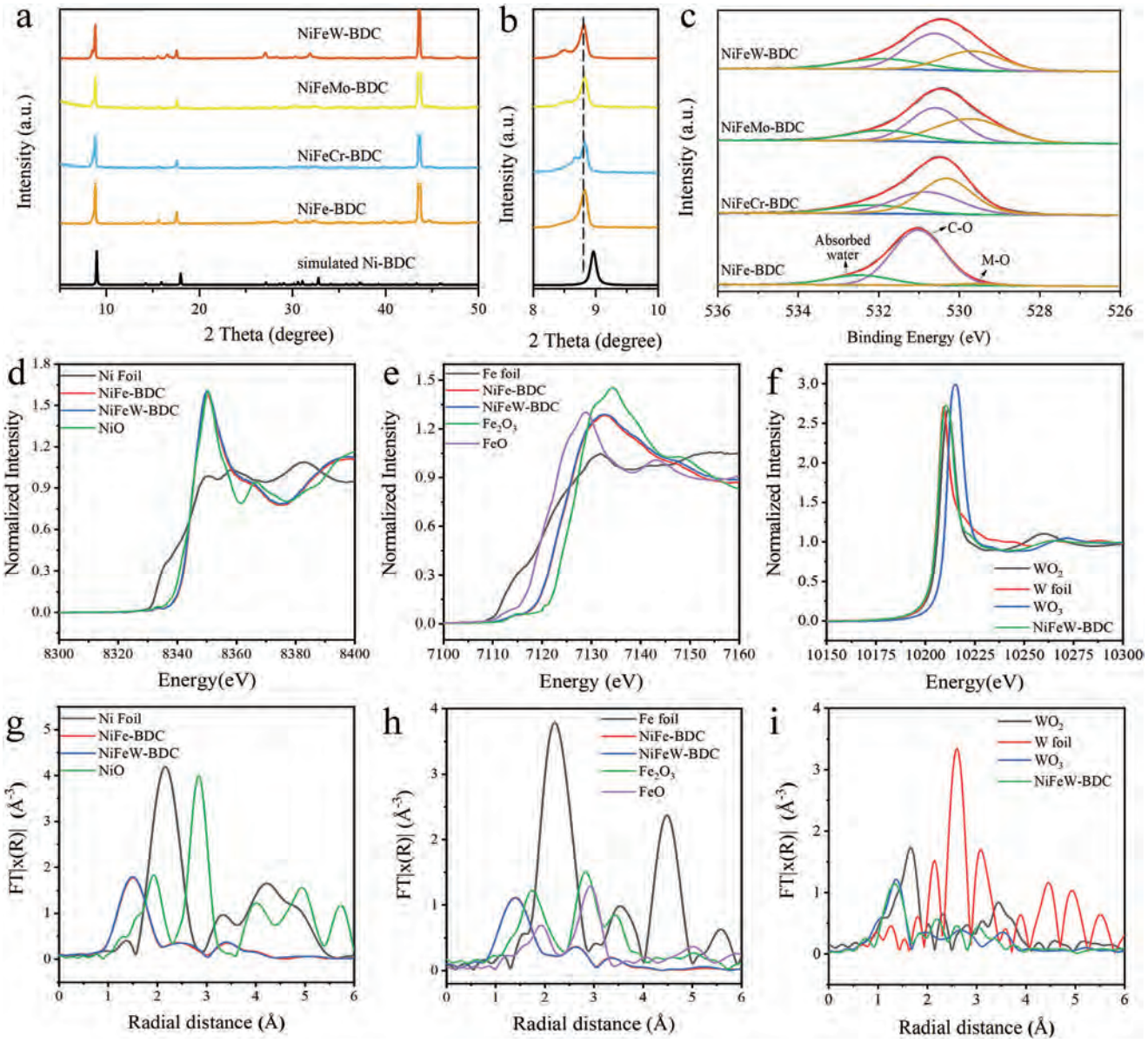

Figure 2. a) XRD pattern, b) enlarged XRD pattern and c) O 1s XPS spectrum of NiFeM-BDC and NiFe-BDC, respectively. d) Ni K-edge, e) Fe K-edge, and f) W L-edge spectra of NiFeW-BDC, NiFe-BDC, and reference samples. g–i) Fourier-transform EXAFS K3-weighted spectra of NiFeW-BDC and reference samples.

doping: substitutional doping and interstitial doping. Based on above analysis: (1) the trace amount of W in the final electrocatalyst, no new phases containing W were observed in the XRD pattern and the totally different coordination number (2.7 ± 0.6) with that of oxide (6), indicating W is in the dopant form rather than the oxide, (2) the coordination number of the W (2.7 ± 0.6) is entirely different with the Ni (6.4 ± 1.4) and Fe (4.6 ± 0.3), confirming the W is not a substitutional dopant replacing Ni or Fe sites. Thus, the W can only be in the form of interstitial dopant in the final electrocatalyst.

To shed light on the effect of various metalates on electrochemical performance, we assessed the cyclic voltammetry (CV) curves of NiFeM-BDC in a standard three-electrode electrolyte with 1 M KOH as the electrolyte (**Figure** 3a). The catalytic activity of NiFeM-BDC was found to follow the order of NiFeW-BDC > NiFeMo-BDC > NiFeCr-BDC > NiFe-BDC in the absence of IR compensation. NiFeW-BDC exhibits superior OER performance compared to other electrocatalysts; only an overpotential of 192, 300, and 730 mV is required to achieve a current density of 10, 100, and 500 mA cm^{-2}, respectively, which is significantly smaller than that of NiFe-BDC (210, 557, and 1176 for the same current densities of 10, 100, and 500 mA cm^{-2}, respectively). Figure 3b provides detailed overpotential data necessary to achieve the current density of 200 and 500 mA cm^{-2}. It should be noted here all nickel foam substrates were prepared using a laser cutting machine, and the CV results of each sample were based

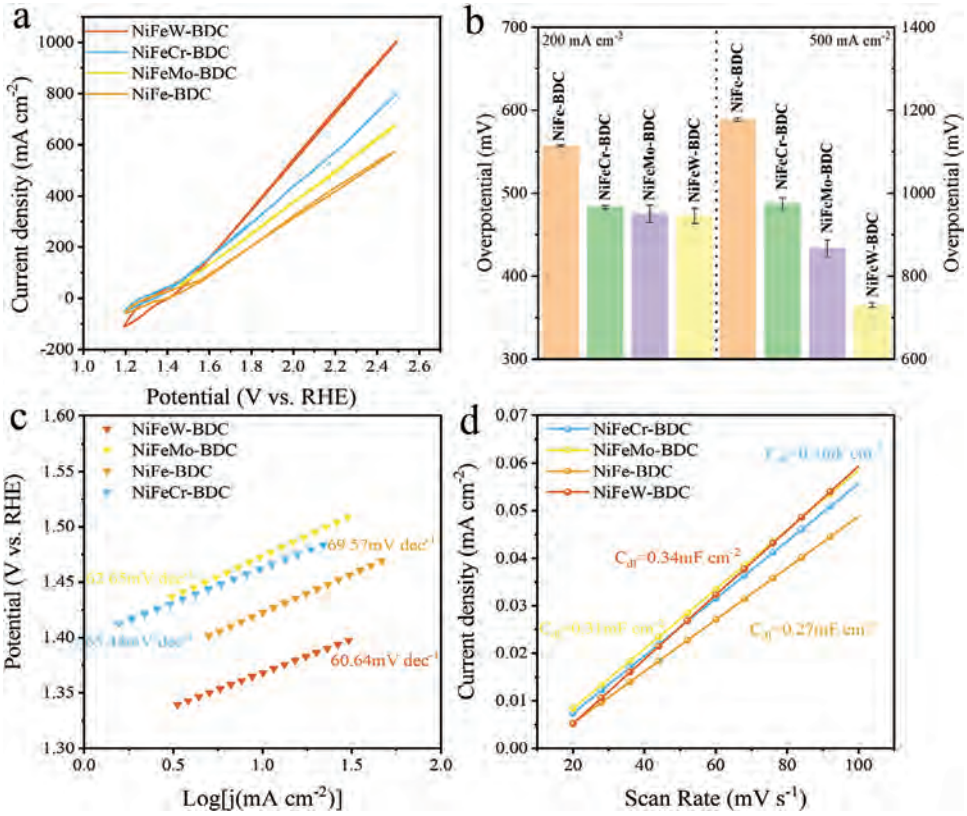

Figure 3. a) CV curves and b) overpotential of NiFeM-BDC and NiFe-BDC for the current density of 200 mA cm^{-2} and 500 mA cm^{-2}; c) Tafel slope and d) C_{dl} values of NiFeM-BDC and NiFe-BDC.

on five separate tests (Figure S2, Supporting Information). In addition, the Tafel slope shown in Figure 3c indicates that NiFeW-BDC has the lowest Tafel slope value (60.64 mV dec^{-1}), followed by NiFeMo-BDC (65.44 mV dec^{-1}) and NiFeCr-BDC (62.65 mV dec^{-1}), suggesting a fast reaction kinetics.[20] The electrochemical active surface area (ECSA) of these electrocatalysts is obtained by analyzing the CV curves in the non-Faraday region, and the results indicate that NiFeW-BDC has the highest ECSA (Figure 3d; Figure S3, Supporting Information). Then, the actual intrinsic activities of the catalysts are determined by normalizing the current density with ECSA (Figure S4, Supporting Information). Clearly, NiFeW-BDC has the highest intrinsic activity among all these electrocatalysts.[21] Moreover, Nyquist plots demonstrate a comparable pattern where NiFeW-BDC/NF displays the lowest charge transfer resistance of 0.05 Ω (Figure S5, Supporting Information), consistent with the Tafel slope analysis.[22]

Since introducing metalate into the MOFs can effectively modulate the catalytic activity, better catalytic performance may be achieved by adjusting the dopant concentration. Besides the role of hydroxide ions in the alkaline hydrolysis of MOFs, metallic acid, an inorganic compound, also undergoes hydrolysis when it is in an aqueous solution. Taking Na_2WO_4 as an example, the WO_4^{2-} ion initially undergoes hydrolysis with water to produce H_2WO_4. Due to the weak acidity characteristics of H_2WO_4, it partially dissociates in water to create H^+ and WO_4^{2-}, which is in a state of dynamic equilibrium (Equations 2 and 4). Therefore, regulating the degree of dissociation of Na_2WO_4 by pH is a practical and feasible approach for controlling the concentration of W and the doping ratio in NiFe BDC.

$$2H_2WO_4 + 4H_2O \leftrightharpoons WO_4^{2-} + 4H_3O^+ \quad (4)$$

To validate this hypothesis and its controllability, we adjusted the pH of the Na_2WO_4 solution from 8 to 14 using 6 M KOH. The SEM images (**Figure** 4a–f) show that the hydroxide ion concentration significantly affects the NiFe-BDC surface morphology. The stacking layer structure became more prominent in the pH range of 9–12. In contrast, when the pH value is increased to 13, excessive hydroxide ion concentrations lead to the collapse of the nanosheet skeleton stacking layers. The impact of pH on the morphology of NiFe-BDC is predominantly a result of the acid-base reaction. This reaction leads to the destruction of the organic linker and the sequestration of metal ions, which in turn etches the nanosheet (Equation 3).[23] When the pH value reaches a critical point, the MOF surface will be selectivity destroyed, making the crystallographic directions richer. Thus, when the catalyst is in situ prepared on the surface of nickel foam, this destruction of the surface selectivity will make the stacking-layer structure disappear and significantly reduce the specific surface area. Moreover, due to the final nickel-containing catalysts prepared on the nickel foam, to avoid the interference of nickel foam on ICP analysis, wherein the atomic ratio of W element obtained via the ICP technique is normalized by Fe element (atomic ratio of W/Fe) to make a side-by-side comparison between different samples.

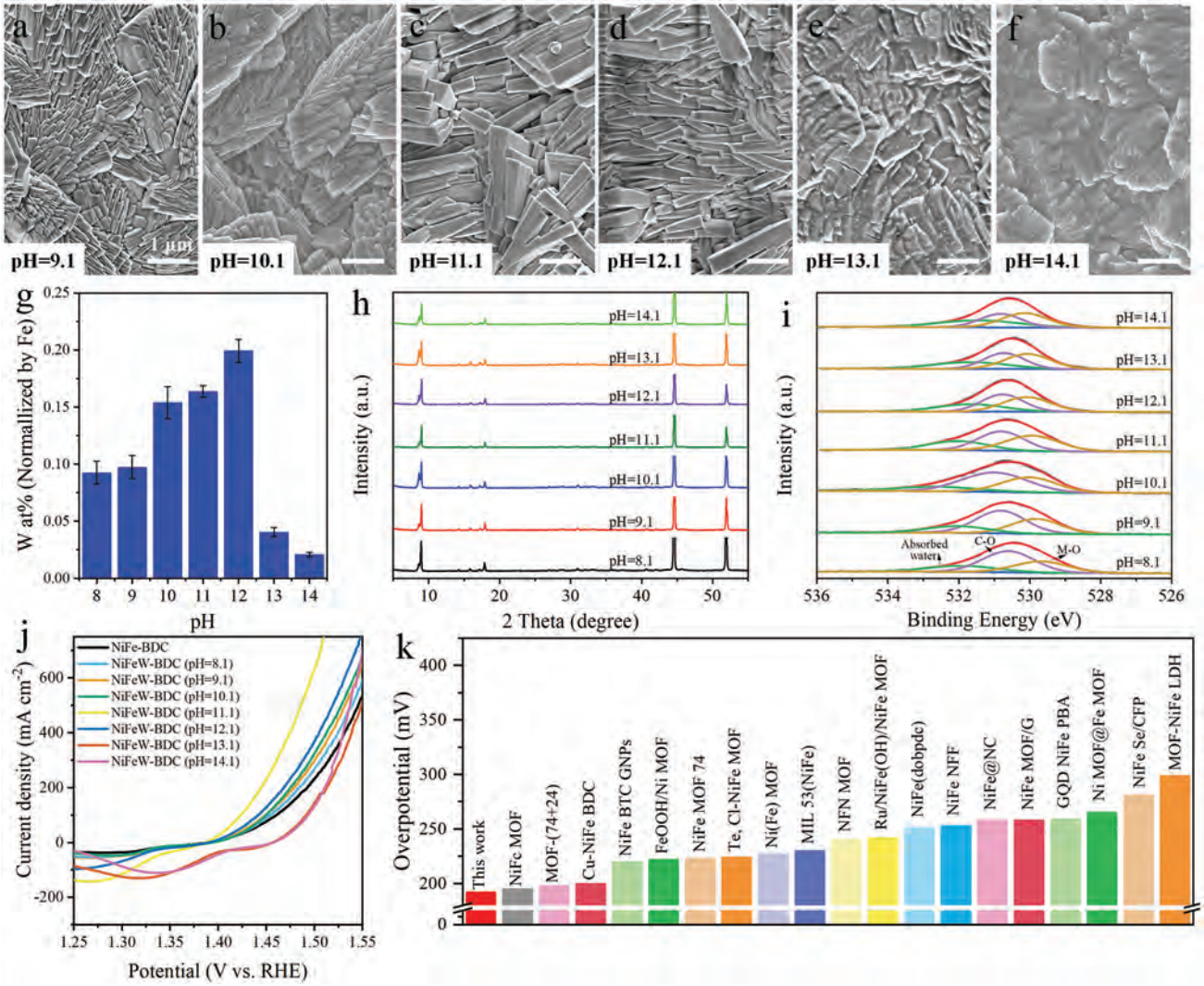

Figure 4. a–f) SEM images of the NiFeW-BDC samples prepared at pH 9.1, 10.1, 11.1, 12.1, 13.1, and 14.1, respectively. g) The W atomic ratio normalized by the Fe element; h) XRD pattern and i) O 1s XPS spectra of the NiFe-BDC and NiFe-BDC, respectively. j) The liner sweeping voltammetry curves of the catalyst fabricated at different pH values; k) Electrochemical performance comparison at the current density of 10 mA cm^{-2} among recently reported NiFe-MOF-based materials.

The atomic ratio between W/Fe elements increases with the increasing pH value, reaching a maximum value of ≈0.2 at pH 12.1, followed by a decrease in the atomic ratio as the pH continues to increase (Figure 4g). In addition, since the nickel foam proceeded to corrode during the hydrothermal process with the existence of Fe ions, the nickel foam dissolved into nickel ions.[24] Thus, though the Ni/Fe ratio in the precursor is 1:2, the atomic ratio of W in the final electrocatalyst is smaller than the range 0.06 at% (pH = 8) ≈ 0.12 at% (pH = 12). Meanwhile, XRD results indicate that the post-alkaline treatment influences the surface morphology of MOF rather than its crystal structure (Figure 4h). The O 1s spectrum results in the enhanced hydroxide concentration, yielding an improved amount of metal hydroxide content in the final product, further indicating introducing metalates into the MOFs alkaline hydrolysis reaction can achieve a modification of morphology and composition in a wide pH range (Figure 4i). Then, for the W 4f spectrum, with the surface LDHs concentration increasing, the binding energy exhibits an apparent blue shift, which may be due to the enhanced electronic interaction between the W and LDHs (Figure S6, Supporting Information). Then, the electrochemical performance in Figure 4j clearly demonstrates the activity can be adjusted via pH, in which when the pH is 11, the NiFeW-BDC exhibits the best performance; only 188.36, 235.9, and 299.1 mV is needed to achieve the 10, 100 and 400 mA cm^{-2} with a Tafel slope of 51.1 mV dec^{-1} (Figure S7, Supporting Information). The superior OER performance of NiFeW-BDC outperforms most of the recently reported NiFe-based electrocatalysts (Figure 4k).[25–43] Although the trend in electrochemical performance does not align with the variation in atomic ratio, the superior electrochemical performance is likely due to the optimized ratio of dopants and the improved surface area.

Due to the superior OER performance of NiFeW-BDC in the alkaline solution, an AEMWE water electrolysis is assembled with the fabricated NiFeW-BDC as the anode and homemade NiFe/Pt

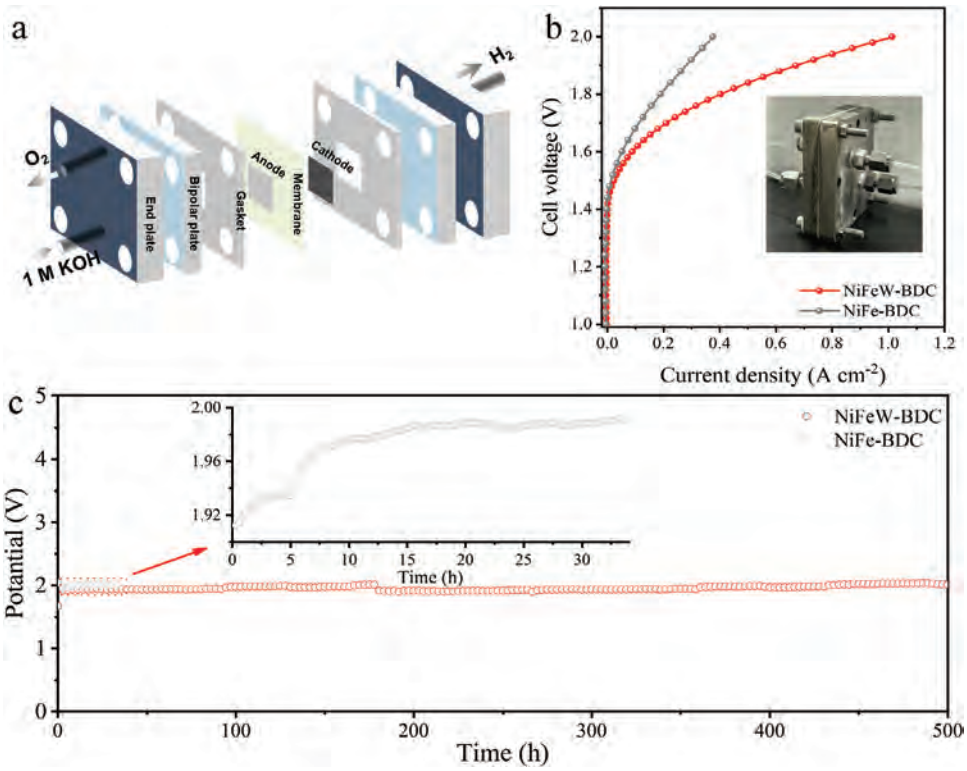

Figure 5. a) Schematic illustration of the AEM electrolyzer; b) Polarization curves of the NiFe-BDC and NiFeW-BDC in the AEM electrolyzer; c) Chronopotentiometry test at 1000 mA cm^{-2} in the AEM electrolyzer.

LDHs as the cathode (**Figure 5**a; Figure S8, Supporting Information). As shown in Figure 5b, the overall water-splitting performance of the NiFe-BDC and NiFeW-BDC was evaluated at room temperature. To achieve the current density of 10, 500, and 1000 mA cm^{-2}, NiFeW-BDC only requires the potential of 1.47, 1.84, and 1.99 V, which is much smaller than of the original NiFe-BDC (375.34 mA cm^{-2} for 2 V). More importantly, the catalyst maintained a stable voltage of 2 V for over 500 h without significant changes at a constant current density of 1000 mA cm^{-2}, confirming the excellent electrochemical stability of NiFeW-BDC and the ultrastable performance in the large current density should be attributed to the protection of LDHs on the MOFs surface (Figure 5c). Furthermore, the SEM, XRD, and XPS results of the catalyst after stability were characterized; the results showed the NiFeW-BDC still kept layer nanostructure, and in situ reconstruction occurred in the electrochemical oxidation environment, exhibiting amorphous characteristics (Figures S9–S11, Supporting Information).

To gain further insight into the underlying synergistic effect between the multi-component on electronic structure as well as the catalytic activity from orbital scale, density functional theory (DFT) computations were performed. First, the interstitial W-doped NiFe-LDHs/MOFs crystal structure was optimized based on the XANES and EXAFS results (**Figure 6**a, b; Figure S12, Supporting Information).[44] The optimized LDHs/MOFs theoretical model was based on the data from Cambridge Structure Database.[45] In addition, the M-OH and M-OOH characteristic vibration peaks are observed during the electrochemical process with the in situ Raman characterization (Figure S13, Supporting Information).[46,47] Thus, to evaluate the OER catalytic performance and the active sites of these models, the Gibbs free energy profiles of the four-electron pathway for each surface with intermediates (i.e., OH*, O*, and OOH*) at alkaline conditions were investigated, which are shown in Figure 6c (Supplementary Computational detail).[48] At $U = 0$, NiFe-BDC's potential determining step (PDS) is the last electron transferred step with an energy change of 2.17 eV, in which adsorbed OOH* reacts with additional OH^- to form O_2 and H_2O. Due to excessively strong adsorption of OOH* intermediate (difficult to form O_2 and H_2O), the NiFe-BDC exhibits a high theoretical overpotential of 0.94 V. Obviously, the addition of W can significantly weaken the adsorption of all intermediate (G_{OH*}, G_{O*}, and G_{OOH*} from 0.27, 1.00 and 2.75 eV to 1.01, 2.19 and 3.82 eV) and thus facilitate the OER process. The PDS of NiFeW-BDC is changed to the formation of adsorbed OOH*, and the overpotential markedly decreases to 0.40 V. In comparison, introducing Cr leads to excessively strong adsorption of reaction intermediates, while the NiFeMo-BDC shows too weak affinity to intermediates. Hence, due to either too strong or too weak binding energy for intermediates, NiFeCr-BDC and NiFeMo-BDC possess high theoretical overpotentials of 1.08 and 0.82 V, respectively. Evidently, the above results indicate that introducing W can effectively modulate the adsorption of intermediates, thus enhancing the OER catalytic activity, which agrees well with the experimental results.

In order to reveal the enhanced mechanism of NiFeW-BDC on OER activity, the electronic properties, including the projected density of states (PDOS), projected crystal orbital Hamilton population (pCOHP), and charge transfer analysis, were calculated.

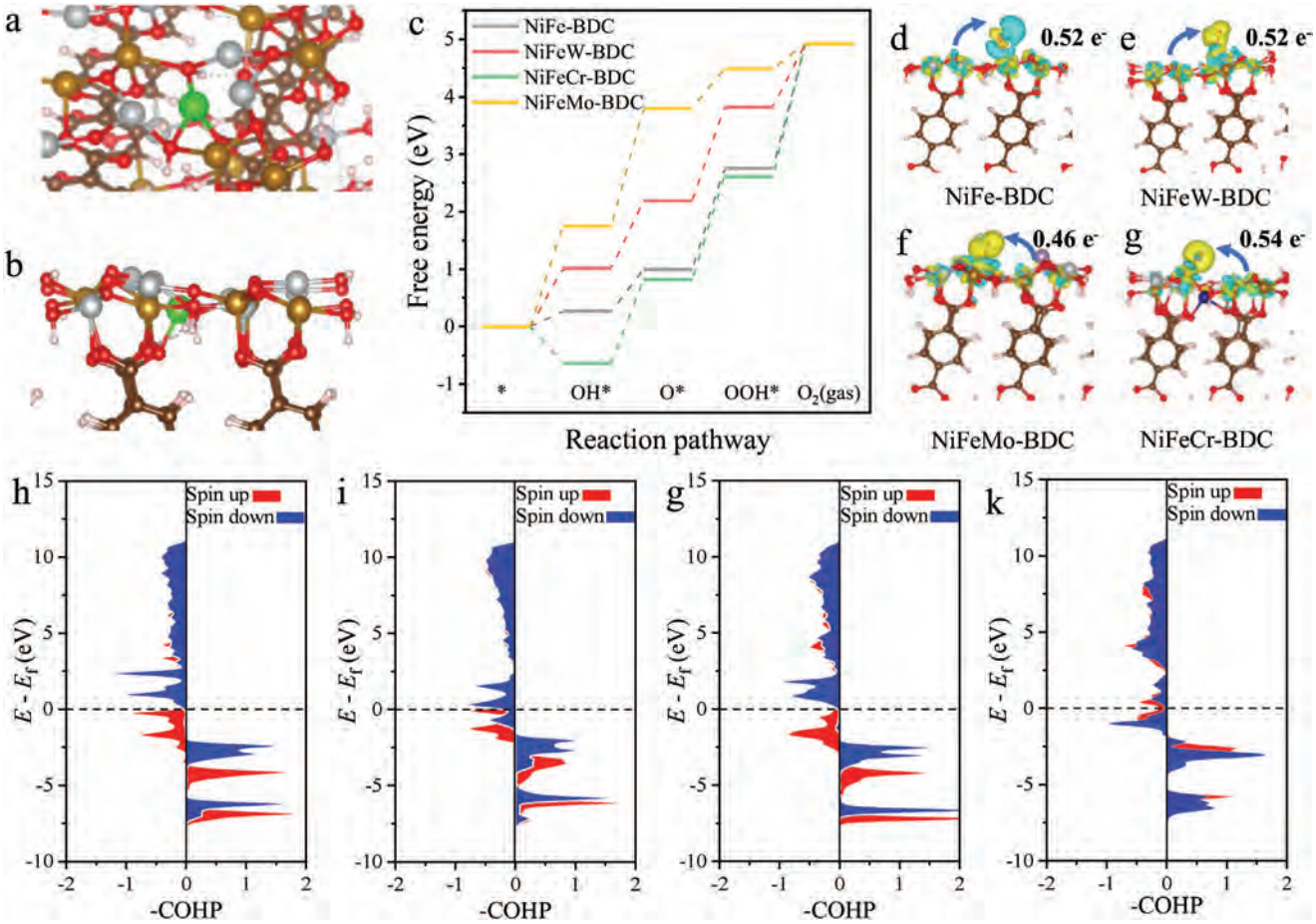

Figure 6. a, b) Optimized structure of NiFeW-BDC; c) Free energy diagram of OER for NiFeM-BDC and NiFe-BDC (M = W, Mo, and Cr); d, e) Electron transfer diagram between the electrocatalyst surface and OH* intermediate (yellow and cyan clouds indicating charge density accumulation and depletion, and isosurface values are set at $\pm 2.0\times10^{-4}$ e Å^{-3}); h–k) pCHOP for OH* adsorbed on NiFe-BDC, NiFeMo-BDC, NiFeCr-BDC and NiFeW-BDC, respectively.

As the adsorption of OH* is the first step and the adsorption energy scaling relation in OER, we will focus on this step in the following discussions. The bonding between the active center and OH* is dominated by their 3d orbitals and p orbitals. Based on the orbital symmetry, the strong σ and σ* bonds can be formed by the hybridization between the d_{z2} and p_z orbitals, while the weak π and π* bonds can be formed by the hybridization between the $d_{xz/yz}$ and $p_{x/y}$ orbitals.[49,50] From PDOS shown in Figure S14 (Supporting Information), it is noted that dz^2, d_{xz}, and d_{yz} orbitals of Ni or Fe atoms are well overlapped with the p orbitals of O in OH*, suggesting that these orbital hybridizations determine the adsorption strength of OH*, and finally affect the OER activity. The NiFe-BDC and NiFeCr-BDC exhibit more stable bonding states with lower energy, validating its stronger affinity to OH*. Compared to NiFeW-BDC, which has suitable bonding states, NiFeMo-BDC has bonding states that are too high, which would hinder the adsorption of OH*. The charge analysis can further clarify bonding properties. Similarly, adsorbed OH* accepts a moderate electron of 0.52 e$^-$ for the NiFeW-BDC system (Figure 6d–g). Additionally, the adsorption of OH* can be reflected by pCOHP analysis, which is widely used to investigate the bonding and anti-bonding contribution quantitatively.[44,51] As depicted in Figure 6h–k, all of the bonding of d-p hybridized orbitals are located below the Fermi level, indicating that these orbitals are full-filled, while the anti-bonding is half-filled. NiFeMo-BDC model yields the largest ICOHP (integrated COHP) values with an order of NiFeMo-BDC (−2.61 eV) > NiFeW (−2.85 eV) > NiFe (−2.87 eV) > NiFeCr (−2.91 eV). This suitable ICOHP for NiFeW suggests a reasonable bonding affinity to OH*, thus boosting the OER activity. According to our DFT results, it is concluded that the superior catalytic activity of NiFeW-BDC is attributed to the optimization of the electronic structures induced by W doping and their corresponding effects on the adsorption/desorption of intermediate (OH*, O*, and OOH*).

3. Conclusion

In summary, VIB metalates (including Na_2WO_4, Na_2CrO_4, and Na_2MoO_4) are adopted as a versatile toolbox to trigger the MOFs/LDHs topological conversion to fabricate a series of OER catalysts. Based on XRD, XPS, XANES, and EXAFS characterization results, the metalates played a vital role in the alkaline hydrolysis process of NiFe-BDC, resulting in the generation of interstitial M-doped NiFe-LDHs/MOFs. Furthermore, varying the

pH value could significantly modify the catalysts' composition, morphology, and electronic structure by regulating the hydrolysis of metalates and MOFs. The final optimized interstitial W-doped NiFe LDHs/MOFs demonstrated superior catalytic performance, with overpotentials of only 250 mV at current densities of 500 mA cm^{-2}. Moreover, the homemade AEMWE could operate stably at a current density of 1 A cm^{-2} for 500 hours. The excellent catalytic activity and stability can be attributed to the optimized intermediate adsorption/desorption behavior and the unique LDHs/MOFs nanostructure. Our work not only demonstrates the potential of interstitial W-doped NiFe LDHs/MOFs for practical applications but also provides a new design approach for modulating MOFs by alkaline hydrolysis strategy.

Supporting Information

Supporting Information is available from the Wiley Online Library or from the author.

Acknowledgements

Y.B., X.L., and H.Z. contributed equally to the work. This work was financially supported by the Chengdu-CAS Science and Technology Cooperation Program (E33YQ225), Shanghai Carbon Neutralization Project (21DZ1207901), Sichuan Science and Technology Program (2024NSFSC1141), the Guangdong Basic and Applied Basic Research Foundation (2023A1515110920), City University of Hong Kong (project no. 7005944 and 9229138) and Shanghai Sailing Program (23YF1455000).

Conflict of Interest

The authors declare no conflict of interest.

Data Availability Statement

The data that support the findings of this study are available from the corresponding author upon reasonable request.

Keywords

electrocatalyst, group VIB metalate, metal-organic framework, oxygen evolution reaction, topological conversion

Received: April 29, 2024
Revised: July 2, 2024
Published online: July 18, 2024

[1] F. Razmjooei, T. Morawietz, E. Taghizadeh, E. Hadjixenophontos, L. Mues, M. Gerle, B. D. Wood, C. Harms, A. S. Gago, S. A. Ansar, K. A. Friedrich, *Joule* **2021**, *5*, 1776.
[2] C. Yang, G. Rousse, K. Louise Svane, P. E. Pearce, A. M. Abakumov, M. Deschamps, G. Cibin, A. V. Chadwick, D. A. Dalla Corte, H. Anton Hansen, T. Vegge, J. M. Tarascon, A. Grimaud, *Nat. Commun.* **2020**, *11*, 1378.
[3] J. H. Kim, D. H. Youn, K. Kawashima, J. Lin, H. Lim, C. B. Mullins, *Appl. Catal. B Environ.* **2018**, *225*, 1.
[4] J. Shan, C. Guo, Y. Zhu, S. Chen, L. Song, M. Jaroniec, Y. Zheng, S. Z. Qiao, *Chem* **2019**, *5*, 445.
[5] Y. P. Zhu, Y. Jing, A. Vasileff, T. Heine, S. Z. Qiao, *Adv. Energy Mater.* **2017**, *7*, 1602928.
[6] G. Cai, W. Zhang, L. Jiao, S. H. Yu, H. L. Jiang, *Chem* **2017**, *2*, 791.
[7] G. Yilmaz, K. M. Yam, C. Zhang, H. J. Fan, G. W. Ho, *Adv. Mater.* **2017**, *29*, 1606814.
[8] T. Deng, Y. Lu, W. Zhang, M. Sui, X. Shi, D. Wang, W. Zheng, *Adv. Energy Mater.* **2018**, *8*, 1702294.
[9] X.-Y. Yu, Y. Feng, Y. Jeon, B. Guan, X. W. D. Lou, U. Paik, *Adv. Mater.* **2016**, *28*, 9006.
[10] J. Li, W. Huang, M. Wang, S. Xi, J. Meng, K. Zhao, J. Jin, W. Xu, Z. Wang, X. Liu, Q. Chen, L. Xu, X. Liao, Y. Jiang, K. A. Owusu, B. Jiang, C. Chen, D. Fan, L. Zhou, L. Mai, *ACS Energy Lett.* **2019**, *4*, 285.
[11] Y. V. Kaneti, J. Tang, R. R. Salunkhe, X. Jiang, A. Yu, K. C. W. Wu, Y. Yamauchi, *Adv. Mater.* **2017**, *29*, 1604918.
[12] Y. Wang, S. Wang, Z. L. Ma, L. T. Yan, X. B. Zhao, Y. Y. Xue, J. M. Huo, X. Yuan, S. N. Li, Q. G. Zhai, *Adv. Mater.* **2022**, *34*, 2107488.
[13] J. Łuczak, M. Kroczewska, M. Baluk, J. Sowik, P. Mazierski, A. Zaleska-Medynska, *Adv. Colloid Interface Sci.* **2023**, *314*, 102864.
[14] G. Wang, D. Huang, M. Cheng, S. Chen, G. Zhang, L. Lei, Y. Chen, L. Du, R. Li, Y. Liu, *Coord. Chem. Rev.* **2022**, *460*, 214467.
[15] J. Huo, Y. Wang, L. Yan, Y. Xue, S. Li, M. Hu, Y. Jiang, Q. G. Zhai, *Nanoscale* **2020**, *12*, 14514.
[16] X. Bu, R. Wei, W. Gao, C. Lan, J. C. Ho, *J. Mater. Chem. A* **2019**, *7*, 12325.
[17] P. Y. Chen, M. Liu, T. M. Valentin, Z. Wang, R. Spitz Steinberg, J. Sodhi, I. Y. Wong, R. H. Hurt, *ACS Nano* **2016**, *10*, 10869.
[18] Y. Tang, L. Dong, H. Bin Wu, X. Y. Yu, *J. Mater. Chem. A* **2021**, *9*, 1456.
[19] Q. Li, Y. Li, J. Zhao, S. Zhao, J. Zhou, C. Chen, K. Tao, R. Liu, L. Han, *J. Power Sources* **2019**, *430*, 51.
[20] B. M. Hunter, H. B. Gray, A. M. Müller, *Chem. Rev.* **2016**, *116*, 14120.
[21] H. Wang, S. Min, Q. Wang, D. Li, G. Casillas, C. Ma, Y. Li, Z. Liu, L. J. Li, J. Yuan, M. Antonietti, T. Wu, *ACS Nano* **2017**, *11*, 4358.
[22] J. Zhang, H. B. Tao, M. Kuang, H. Bin Yang, W. Cai, Q. Yan, Q. Mao, B. Liu, *ACS Catal.* **2020**, *10*, 8597.
[23] W. Li, S. Xue, S. Watzele, S. Hou, J. Fichtner, A. L. Semrau, L. Zhou, A. Welle, A. S. Bandarenka, R. A. Fischer, *Angew. Chem. – Int. Ed.* **2020**, *59*, 5837.
[24] X. Bu, R. Wei, Z. Cai, Q. Quan, H. Zhang, W. Wang, F. Li, S. Po, Y. Meng, K. Sum, X. Wang, *Appl. Surf. Sci.* **2021**, *538*, 147977.
[25] K. Rui, G. Zhao, Y. Chen, Y. Lin, Q. Zhou, J. Chen, J. Zhu, W. Sun, W. Huang, S. X. Dou, *Adv. Funct. Mater.* **2018**, *28*, 1801554.
[26] D. Liu, H. Xu, C. Wang, C. Ye, R. Yu, Y. Du, *J. Mater. Chem. A* **2021**, *9*, 24670.
[27] K. Park, J. Kwon, S. Jo, S. Choi, E. Enkhtuvshin, C. Kim, D. Lee, J. Kim, S. Sun, H. S. Han, T. Song, *Chem. Eng. J.* **2022**, *439*, 135720.
[28] C. Ni, H. Zheng, W. Liu, L. Wu, R. Li, K. Zhou, W. Zhang, *Adv. Funct. Mater.* **2023**, *33*, 2312764.
[29] P. Thangavel, M. Ha, S. Kumaraguru, A. Meena, A. N. Singh, A. M. Harzandi, K. S. Kim, *Energy Environ. Sci.* **2020**, *13*, 3447.
[30] Y. Wang, B. Liu, X. Shen, H. Arandiyan, T. Zhao, Y. Li, M. Garbrecht, Z. Su, L. Han, A. Tricoli, C. Zhao, *Adv. Energy Mater.* **2021**, *11*, 2003759.
[31] M. Salmanion, M. M. Najafpour, *Int. J. Hydrogen Energy* **2021**, *46*, 19245.
[32] J. Wang, Y. Jiang, C. Liu, Y. Wu, B. Liu, W. Jiang, H. Li, G. Che, *J. Colloid Interface Sci.* **2022**, *614*, 532.
[33] L. Du, L. Luo, Z. Feng, M. Engelhard, X. Xie, B. Han, J. Sun, J. Zhang, G. Yin, C. Wang, Y. Wang, Y. Shao, *Nano Energy* **2017**, *39*, 245.
[34] J. Ding, D. Guo, N. Wang, H. F. Wang, X. Yang, K. Shen, L. Chen, Y. Li, *Angew. Chem. – Int. Ed.* **2023**, *62*, 202311909.
[35] Y. Guo, C. Zhang, J. Zhang, K. Dastafkan, K. Wang, C. Zhao, Z. Shi, *ACS Sustainable Chem. Eng.* **2021**, *9*, 2047.

[36] L. Qi, Y. Q. Su, Z. Xu, G. Zhang, K. Liu, M. Liu, E. J. M. Hensen, R. Y. Y. Lin, *J. Mater. Chem. A* **2020**, *8*, 22974.
[37] S. Jiang, M. Wu, Z. Xu, J. Zhao, R. Liu, *Colloids Surf. A Physicochem. Eng. Asp.* **2023**, *677*, 132400.
[38] Y. Jiang, T. Y. Chen, J. L. Chen, Y. Liu, X. Yuan, J. Yan, Q. Sun, Z. Xu, D. Zhang, X. Wang, C. Meng, X. Guo, L. Ren, L. Liu, R. Y. Y. Lin, *Adv. Mater.* **2024**, *36*, 2306910.
[39] D. Senthil Raja, X. F. Chuah, S. Y. Lu, *Adv. Energy Mater.* **2018**, *8*, 1870105.
[40] C. Cao, D. D. Ma, Q. Xu, X. T. Wu, Q. L. Zhu, *Adv. Funct. Mater.* **2019**, *29*, 1807418.
[41] F. Hu, D. Yu, W. J. Zeng, Z. Y. Lin, S. Han, Y. Sun, H. Wang, J. Ren, S. F. Hung, L. Li, S. Peng, *Adv. Energy Mater.* **2023**, *13*, 2301224.
[42] Y. C. Lin, S. Aulia, M. H. Yeh, L. Y. Hsiao, A. M. Tarigan, K. C. Ho, *J. Colloid Interface Sci.* **2023**, *648*, 193.
[43] F. Sun, G. Wang, Y. Ding, C. Wang, B. Yuan, Y. Lin, *Adv. Energy Mater.* **2018**, *8*, 1800584.
[44] Z. Li, X. Zhang, Y. Kang, C. C. Yu, Y. Wen, M. Hu, D. Meng, W. Song, Y. Yang, *Adv. Sci.* **2021**, *8*, 2002631.
[45] E. L. Markun, D. A. Jensen, J. D. Vegetabile, J. A. Kaduk, *Cryst. Commun.* **2022**, *78*, 584.
[46] N. Zhang, S. X. Guan, Q. Zhang, J. R. Zhao, J. Y. Zhang, Q. F. Ke, Y. Z. Fang, *Chem. Eng. J.* **2023**, *473*, 145223.
[47] F. Tang, T. Liu, W. Jiang, L. Gan, *J. Electroanal. Chem.* **2020**, *871*, 114282.
[48] J. Joo, T. Kim, J. Lee, S. Il Choi, K. Lee, *Adv. Mater.* **2019**, *31*, 1806622.
[49] X. Meng, C. Ma, L. Jiang, R. Si, X. Meng, Y. Tu, L. Yu, X. Bao, D. Deng, *Angew. Chem. – Int. Ed.* **2020**, *59*, 10502.
[50] B. Bayatsarmadi, Y. Zheng, A. Vasileff, S. Z. Qiao, *Small* **2017**, *13*, 1700191.
[51] Y. H. Wang, L. Li, J. Shi, M. Y. Xie, J. Nie, G. F. Huang, B. Li, W. Hu, A. Pan, W. Q. Huang, *Adv. Sci.* **2023**, *10*, 2303321.